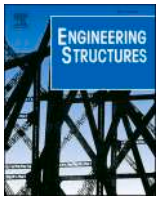
Engineering Structures 329 (2025) 119822



Contents lists available at ScienceDirect

Engineering Structures

journal homepage: www.elsevier.com/locate/engstruct





Flexural behaviour of reinforced concrete slabs strengthened with textile-reinforced strain-hardening cementitious composites subjected to post-strengthening corrosion

Essam Khaled, Ali Hassan *, Mohamed H. Mahmoud, Tarek F. El-Shafiey

Structural Engineering Department, Faculty of Engineering, Tanta University, Tanta, Egypt

ARTICLE INFO

Keywords:
Concrete
Corrosion
Strengthening
Textile fiber
Strain hardening cementitious composite
SHCC

ABSTRACT

Many reinforced concrete (RC) structures are often vulnerable to corrosion damage after strengthening application. This may lead to a high loss in the strengthening efficiency, thus the proper selection of a sustainable strengthening technique could mitigate the corrosion damages. Based on the utilization of textile-reinforced strain-hardening cementitious composites (TR-SHCC), the present work aims to assess the effect of the strengthening regime on the flexural behaviour of RC slabs subjected to post-strengthening accelerated corrosion. The experimental program contained sixteen typical RC slabs divided into four groups. The slabs of group I were kept without any strengthening, whereas the others were strengthened at the tension side with a layer of TR-SHCC. The slabs of group II were strengthened using an externally bonded (EB) layer of 20 mm thickness, without removing the concrete cover. While, groups III and IV were strengthened with a near-surface embedded (NSE) layer of 20 and 35 mm, respectively, the SHCC partially or fully replaced the steel reinforcement cover. After strengthening, three slabs of each group were subjected to different durations of accelerated corrosion (10, 20, and 30 days). Following, the slabs were tested under a four-point bending scheme. The experiments showed that exposing the EB-strengthened slabs to corrosion significantly reduced the ultimate capacity and ductility. In addition, after 30 days of corrosion exposure, the EB-strengthening showed an insignificant effect on the slab capacity. Compared to other regimes, the NSE-strengthening with a full SHCC-replaced cover was more efficient in decreasing the corrosion rate and controlling the loss in the strengthening efficiency. A prediction model for the ultimate moment of the TR-SHCC-strengthened corroded slabs was proposed. The model gave good results compared to the experimental results.

1. Introduction

In recent years, many RC structures have required strengthening/repair for maintenance, sustainability, overloading, and requirements of modern design code. The most common technique is section enlargement with a new concrete layer. However, this technique is threatened by de-lamination or debonding between the interface between the two layers. The interfacial bond could be improved by good surface roughening or by using shear studs between the two materials [1]. Also, fiber-reinforced polymer (FRP) has been widely used to upgrade the strength of deficient RC elements. This material has many promising advantages, such as corrosion resistance, a high strength-to-weight ratio, ease of application, and minimal change in the section geometry. Despite the high bond strength of epoxy resins, the strengthening layers need anchors to avoid the debonding failure mode. In addition, FRP materials have low fire resistance which adds a fire protection cost [2]. Moreover, epoxy resins have many weak points, such as high cost, inapplicability on wet surfaces and poor thermal compatibility with concrete [2].

Textile-reinforced mortar (TRM) has been widely used for the strengthening/repair of deficient RC elements. The TRM consists of textile polymer fibers embedded into a cementitious matrix. The most common bonding matrices are cement mortar or polymer-modified mortar [3–7]. The ability of TRM composites to improve the structural behaviour of RC elements has been investigated [8,9]. The TRM could avoid many drawbacks of the EB-FRPs, such as incompatibility with substrate concrete, low resistance at high temperatures, and debonding failure at the interface, however, new issues are brought up [10].

* Correspondence to: Tanta University, Tanta 31511, Egypt.
E-mail address: ali_hassan@f-eng.tanta.edu.eg (A. Hassan).

https://doi.org/10.1016/j.engstruct.2025.119822
Received 31 October 2024; Received in revised form 12 December 2024; Accepted 24 January 2025
Available online 1 February 2025
0141-0296/© 2025 Elsevier Ltd. All rights are reserved, including those for text and data mining, AI training, and similar technologies.

Compared to the epoxy-bonded fibers, the ultimate tensile strains of dry fibers were significantly reduced with the use of cementitious mortars [11]. This is owing to the low tensile strain capacity of ordinary cementitious mortars [11]. Recently, strain-hardening cementitious composites (SHCC) have been getting increasing attention because of their superior properties such as high tensile strain capacity and improved cracking behaviour [12]. In previous research different names for the SHCC materials were used, namely: Engineered Cementitious Composite (ECC), High Performance Fiber Reinforced Cementitious Composites (HPFRCC), and Bendable concrete etc. SHCC has a tensile strain capacity of more than 2 % (20,000 με) and a fiber volume of friction (V_f) of less than 2 % [13–17]. In tension, SHCC can display several micro cracks with a crack width of less than 100 μm instead of a single localized fracture crack in traditional cement composites [18]. The improved tensile properties of SHCC gave it leadership in many strengthening and repairing applications, especially when ductility and crack width control are the main requirements [18–23].

Several researchers suggested the use of SHCC material instead of traditional mortar in TRM strengthening. The composite use of FRP and SHCC has many benefits [24,25]. The excellent tensile deformation capacity of the SHCC material can efficiently suppress the poor cracking behaviour of ordinary mortars [24]. In addition, the FRP reinforcement increases the tensile strain capacity of the SHCC [24]. That led to many applications of FRP-SHCC in the field of RC strengthening. Previous work [26] proposed precast FRP-reinforced ECC panels as a stay-in-place formwork for sustainable marine structures. Compared to FRP-reinforced high-strength concrete panels, the FRP-reinforced ECC panels showed higher load-carrying capacity, stiffness, and deformation capacity [26]. Also, Zhu et al. [27] proposed a novel strengthening system for RC beams utilizing a thin layer of ECC layer reinforced with FRP bars. The results revealed the effectiveness of the FRP-reinforced ECC layers in improving the mechanical performance of RC structures [27]. Ellithy et al. [28] evaluated the flexural performance of RC beams strengthened with SHCC layer reinforced with prestressed FRP bars. The SHCC prevented the spalling of the concrete cover and increased the load-carrying capacity by about 26.5 % [28]. In general, based on the previous work, the FRP-SHCC is a promising system in strengthening/repairing RC structures [29,30].

Corrosion is a chemical or electrochemical reaction between steel and the surrounding environment that leads to the degradation of the steel mass and its properties [31–33]. The two main reasons for the corrosion of steel in concrete are the chloride attack and carbon dioxide penetration (carbonation). The corrosion process produces iron oxides and hydroxides which are usually deposited around the steel reinforcement [34–37]. The products of the corrosion process (iron oxides and hydroxides) create expansive stresses around the steel bars, which cause cracking and spalling of concrete cover [38,39]. For RC elements subjected to corrosive environments, the bond strength is greatly affected by reinforcement corrosion and cracks caused by volume expansion [40]. For non-confined steel rebar, increasing the corrosion ratio degenerates the bond strength [40]. A mass loss ratio of around 5 % of unconfined steel rebar reduces about 78 % of bond strength [40]. Hou et al. [41] evaluated the effect of corrosion on the bond behaviour of steel bars embedded in SHCC and concrete samples. Compared to concrete samples, the SHCC showed improved pull-out strength due to the bridging action of fiber in SHCC. In previous work, Şahmaran et al. [42] studied the effect of accelerated corrosion on steel bars embedded in SHCC prisms. The tests showed that the SHCC has a significant anti-spalling resistance compared to ordinary concrete. Moreover, after 24 hours of accelerated corrosion, the flexural capacity of the control concrete beam reduced to about 34 % of its original strength. Whereas, after 50 hours of corrosion exposure, the SHCC beam saved almost 100 % of its original strength [42].

As presented in the previous investigations, the FRP-SHCC strengthening improved the flexural performance of RC elements. However, the effectiveness of this strengthening technique after corrosion exposure is still a critical issue. The current work aims to fill the gap of knowledge on the efficiency of TR-SHCC strengthened RC slabs subjected to post-strengthening accelerated corrosion. In this study, the experimental program contained sixteen RC slabs subdivided into four groups. The first group was kept without any strengthening. On the other hand, groups II, III and IV were strengthened at the tension zone using a TR-SHCC layer employing three different regimes. For group II, the strengthening layer with a thickness of 20 mm was applied in the form of an externally bonded layer (without removing the concrete cover). Where, in the second and third regimes, the strengthening was applied in the form of a near-surface embedded layer. At the tension side of the slabs, first either 20 or 35 mm depth of concrete at the tension side was removed, and then the strengthening layer with the same thickness was applied. When 20 mm thickness of the SHCC was applied (group III), the strengthening layer covered the half-depth of the main reinforcing bars. Whereas, when the thickness of the SHCC was 35 mm (group IV), the SHCC coated the main steel reinforcement of the slab. For each strengthening regime, three slabs were subjected to different durations of accelerated corrosion (10, 20 and 30 days). Afterwards, the slabs were tested under a four-point loading scheme. The flexural test results in terms of loads, failure modes, load-deflection, strains and crack width for the studied slabs were presented and compared with reference uncorroded slabs. Also, a flexural capacity prediction model was proposed and evaluated.

2. Experimental study

2.1. Test program

The summary of the experimental program is presented in Table 1. In the current study, experiments were on sixteen reduced-scale RC slabs, which were designed to fail in flexural tension failure. Fig. 1 shows the details of the studied slabs. As shown in Fig. 1, the original slabs (before strengthening) had the same dimensions of 120 × 375 × 1500 mm^3 (thickness×width×length). The slabs were reinforced in both directions with a bottom layer of steel bars, three high-strength bars of 10 mm diameter in the main longitudinal direction, and eight bars of 10 mm diameter in the secondary transverse direction. The concrete cover was 15 mm.

As presented in Table 1, experiments were carried out into sixteen test slabs, which were subdivided into four groups, four slabs in each. Group I was kept without any strengthening, whereas the remaining groups (II, III, and IV) were strengthened at the tension side with a TR-SHCC layer. The TR-SHCC layer consisted of one layer of textile carbon fiber embedded into SHCC mortar. In group II, the TR-SHCC layer with a thickness of 20 mm was applied in the form of an externally bonded (EB) layer. This group was strengthened without concrete cover removal, thus, after the strengthening application, the total depth of the slabs increased to 140 mm. As for groups III and IV, the slabs were strengthened using near-surface embedded (NSE) layers of 20 and 35 mm thickness, respectively. Before strengthening, 20 or 35 mm of concrete depth was removed and then replaced by SHCC. In group III, the SHCC covered half of the main steel bars. Whereas, in group IV, the SHCC layer coated the steel bars. To evaluate the efficiency of the applied strengthening after corrosion exposure, after 28 days of the strengthening application, three slabs of each group were subjected to three different durations of accelerated corrosion of 10, 20, and 30 days. Then the corroded and un-corroded slabs were tested under flexural loading tests.

As presented in Table 1, the slabs of group I were designated with the letter S followed by the duration of corrosion (0, 10, 20 and 30 days). For instance, slab “S10” refers to an un-strengthened slab subjected to ten days of accelerated corrosion. On the other hand, the strengthened slabs of groups II, III and IV were symbolized in three symbols. The first was similar to that used for group I. The second and third symbols were added to refer to the strengthening regime and the thickness of the

Table 1
Description of test slabs.

Group	Slab ID	Strengthening regime	t, mm	t_{conc}, mm	t_{SHCC}, mm	Duration of accelerated corrosion, day
Group I	S0	Unstrengthened slabs	120	120	-	-
	S10		120	120	-	10
	S20		120	120	-	20
	S30		120	120	-	30
Group II	S0-EB−20	The slabs strengthened with externally bonded TR-SHCC	140	120	20	-
	S10-EB−20		140	120	20	10
	S20-EB−20		140	120	20	20
	S30-EB−20		140	120	20	30
Group III	S0-NSE−20	The slabs strengthened with near surface embedded TR-SHCC that partially coating the main reinforcement	120	100	20	-
	S10-NSE−20		120	100	20	10
	S20-NSE−20		120	100	20	20
	S30-NSE−20		120	100	20	30
Group IV	S0-NSE−35	The slabs strengthened with near surface embedded TR-SHCC that fully coating the main reinforcement	120	85	35	-
	S10-NSE−35		120	85	35	10
	S20-NSE−35		120	85	35	20
	S30-NSE−35		120	85	35	30

t = total thickness of section including the thickness of strengthening if any; t_{conc} = thickness of concrete; t_{SHCC} = thickness of SHCC

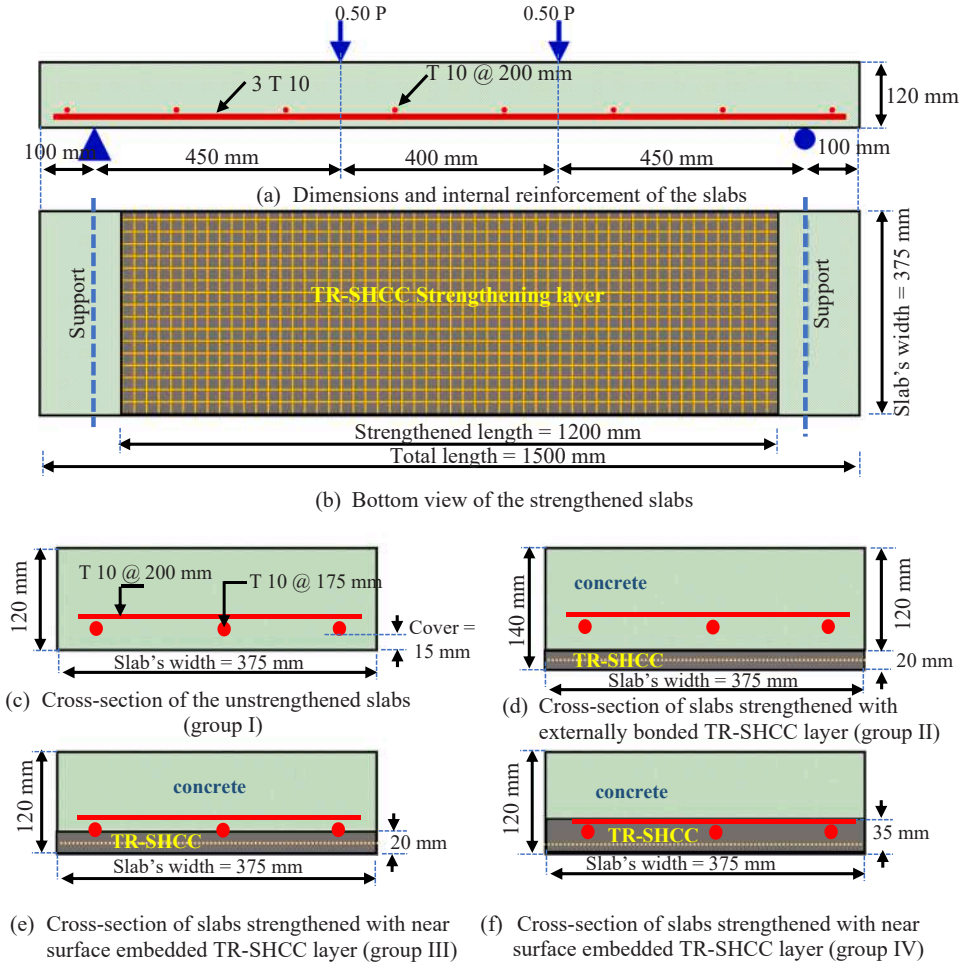


Fig. 1. Details of the studied slabs.

strengthening layer, respectively. For instance, the designation "S10-NSE-35" refers to a test slab strengthened with a near-surface embedded layer with 35 mm thickness and then subjected to 10 days of accelerated corrosion.

2.2. Material properties

Table 2 presents the proportions of the used concrete and SHCC mixtures. In this study, the slabs were cast from the same concrete mixture to obtain similar concrete properties in all specimens. Ordinary Portland cement and a water-to-cement ratio (w/c) of 0.45 was used. Fine sand with a weight of 746 kg/m^3 and crushed stone with a weight of 1082 kg/m^3 were used. Following ASTM C39/C39M [43] and ASTM C496/C496M [44], during the preparation of the slabs, concrete cylinders having a diameter of 150 mm and a height of 300 mm were sampled to measure the compressive and tensile strengths of the used concrete. The material tests were performed at the age of the slab specimens' tests. For the tested cylinders, the mean results of the compressive and tensile strengths of the used concrete were 35 MPa, and 3.63 MPa, respectively.

The SHCC mixture is shown in Table 2. The mixture consists of Ordinary Portland cement (Type I), silica fume with an average size of 0.2 μm, fine silica sand with a size less than 0.2 mm, polypropylene (PP) short fibers with a volume of fraction (V_f) 2 %, water and superplasticizers. As included in the manufacturer's datasheet, the length of the used fibers was 12 mm and the diameter was 25 μm. The fibers had a tensile strength of 2800 MPa with an ultimate strain of 2.52 % and the modulus of elasticity was 115 GPa. Following JSCE recommendations [45], compressive tests were performed on three standard cylinder samples at the same age as the slabs' tests. The diameter of the samples was 50 mm and the height was 100 mm. The average compressive strength of SHCC samples was about 46.6 MPa. Also, the tensile strength of the SHCC material was obtained through uniaxial tensile tests, which were performed on six dumbbell-shaped samples. The dimensions of the tensile test samples are presented in Fig. 2. The samples had a cross-section of 30 × 300 mm^2 and a gauge length of 80 mm. The first cracking and ultimate tensile strengths of the used SHCC were 3.15 and 7.26 MPa, respectively.

In the current study, steel bars with a diameter of 10 mm (type B500DWR) were used for the internal reinforcement of the slabs. Following ASTM E8/E8M [46], tensile tests were performed on three steel samples. The mean yield strength and ultimate strengths of the used steel were 550 and 690 MPa, respectively.

The studied slabs were strengthened using a TR-SHCC layer. The used carbon textile fibers textile is shown in Fig. 3. The textile had an opening mesh with dimensions of 20 × 20 mm^2 and a density of 1.8 g/cm^3. As included the material datasheet, the tensile strength and elongation were 4000 MPa and 1.5 %, respectively.

2.3. Strengthening application

Figs. 4 and 5 show the test slabs during the strengthening application. Beyond 28 days of concrete casting, to facilitate the strengthening work, the slabs were placed upside down (the slab soffit was placed at the top). For group II, as shown in Fig. 4a, the concrete surface was roughened with a needle scaler hammer to create about 5 mm roughening depth. Whereas, for the slabs of groups III and IV, as shown in Figs. 4b and 4c, a depth of 25 or 35 mm of concrete was removed using a sharp silting tool. Afterwards, a high-pressure air jet was used to remove any loose particles or dust from the substrate concrete. Before the SHCC casting, plywood shuttering was fixed at both sides of the slab.

Fig. 5 shows the steps of the TR-SHCC layer application. Firstly, a layer of SHCC was cast, the thickness of this layer was 10 mm for groups II and III and 25 mm for group IV. Then, as shown in Fig. 5, the textile carbon fiber was placed over this layer. Subsequently, the remaining part of the strengthening (10 mm thickness) was cast to cover the textile. The surface was finished after the casting of the TR-SHCC layer. After the TR-SHCC layer consolidation, the strengthened area was cured using wet burlaps for 14 days. Thereafter, the slabs were left in the air for 14 days before exposure to corrosion.

2.4. Accelerated corrosion

Fig. 6 shows the setup of the accelerated corrosion process for the test slabs. As shown in Fig. 6, inside a corrosion tank, each slab was partially submerged inside the electrolyte to a level where the reinforcement was partially submerged in NaCl solution (5 % concentration). The process was accelerated through a DC power supply in a constant current mode operation (32 V, 3 A). As shown in Fig. 6, the DC power supply had positive and negative terminals. The negative terminal (cathode) was connected to a copper plate placed in the electrolyte, while, the positive terminal (anode) was connected to the middle of the steel reinforcement using an electrical wire. The electrical wire was isolated using a coating of silicon. Each slab was subjected to an external current equal to 0.5 A. Three slabs of each group were set in the corrosion tank for three different durations of 10, 20, and 30 days. Following Faraday's law [47], the corrosion mass loss was estimated, as presented in Eq. (1). The expected mass losses in the steel reinforcement after the studied durations are presented in Table 3.

$$m_c = \frac{M \times I \times T}{Z \times F} \quad (1)$$

Where,

m_c = corrosion mass loss (g); M = molar mass of Fe (56 g/mol); I = the current (0.5 A); F = Faraday's constant which equals 96487 C/mol; T = the time by second; Z = ionic number (2 for steel).

2.5. Test setup and instrumentation

The experimental test setup and the instrumentation of the tested slabs are shown in Fig. 7. The slabs were tested under a static load in a four-point bending scheme. The acting load was measured using a recalibrated load cell having a load capacity of 400 kN. The slabs' deflections were measured using five linear variable differential transformers (LVDTs) with an amplitude of 100 mm. As shown in Fig. 7, LVDTs (1), (2) and (3) were placed under the slab at the middle of the span and the loading points. Also, LVDTs (4) and (5) were placed over the supports to measure any possible movement in the supports. The tensile strain of the internal reinforcement and textile carbon fiber were measured by electrical strain gauges (10 mm gauge length). Also, strain gauges of 50 mm gauge length were bonded on the concrete surface of the specimen at different locations to plot the strain distribution over the depth. A digital microscope (an accuracy of 0.01 mm) was used to measure the maximum flexural crack width. The measuring tools (load cell, strain gauges and LVDTS) were linked to an automatic data acquisition system (20-channel data logger) to monitor the test results.

Table 2
The mix proportions of concrete and SHCC for one cubic meter (kg/m^3).

Material	Binder		Aggregate		Fibers (volumetric ratio)	Super plasticizers	Water	Water-to-binder ratio
	Cement	Silica-fume	Fine (Sand)	Coarse (Crushed lime stone)				
Concrete	400	—	746	1082	—	—	180	0.45
SHCC	1342	237	160	—	16.20 (2.0 %)	31.6	312.1	0.20

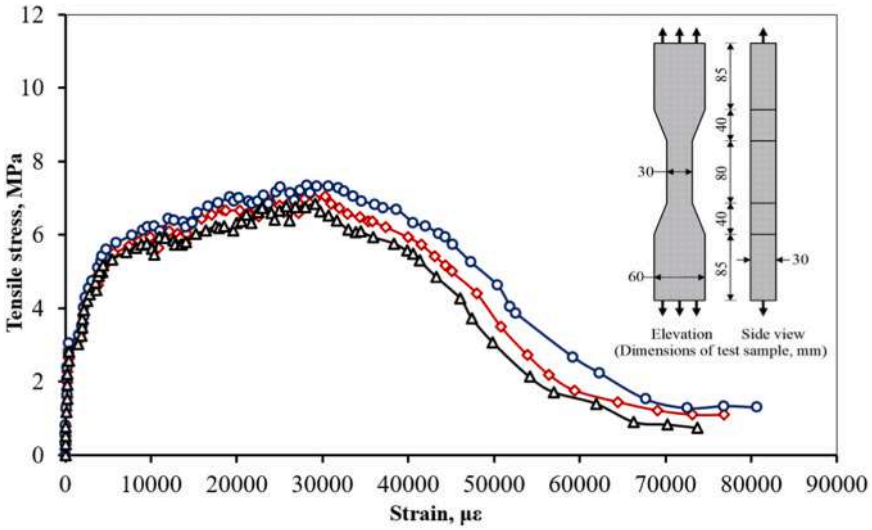


Fig. 2. Stress-strain curves of SHCC under uniaxial tensile test.

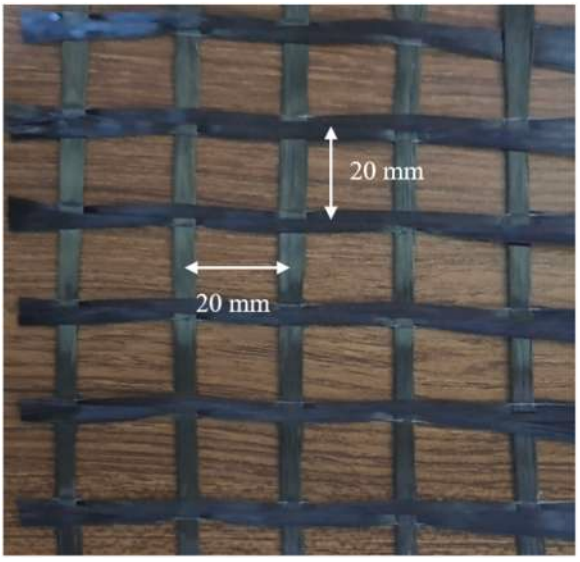
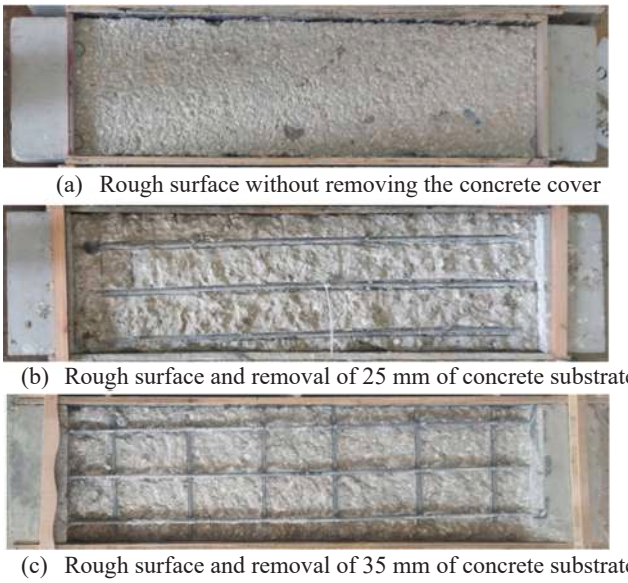


Fig. 3. RThe used textile carbon fiber.



(a) Rough surface without removing the concrete cover

(b) Rough surface and removal of 25 mm of concrete substrate

(c) Rough surface and removal of 35 mm of concrete substrate

Fig. 4. Different conditions of concrete substrate.

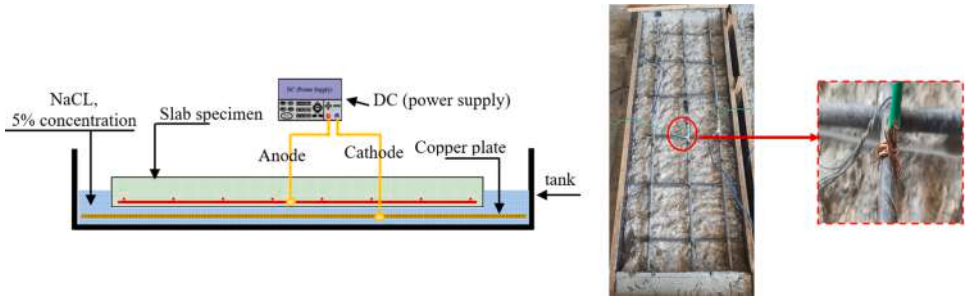
3. Experimental results

3.1. Half-cell test

Following ASTM C876 [48], the half-cell test was carried out during the accelerated corrosion process. As per ASTM C876, if the reading of electrical potential difference reaches the value of −350 mv, the probability of corrosion occurrence is above 90 %. Fig. 8 plots the relation between the readings of the half-cell (mv) and the exposure time (days) for slabs S30 (unstrengthened) and slab S30-NSE-35 (strengthened). As shown in Fig. 8, the electrical potential difference reached −350 mv, at ages of 4 and 22 days for the un-strengthened and strengthened slabs, respectively. At these ages, hair corrosion cracks were noticed in the slabs through visual inspection. This means that the strengthening layer could delay the occurrence of the first corrosion crack by more than 450 %, compared to the un-strengthened one. Also, Fig. 9 plots the relation between the electric current intensity (A) and the exposure time (day) for slabs S30 (unstrengthened) and slab S30-NSE-35 (strengthened with NSE-TR-SHCC). For the un-strengthened slab, the current intensity showed a slight increase until the first corrosion crack appeared then the



Fig. 5. Images during the application of the TR-SHCC layer.



(a) Sketch of setup (b) Image of anode-bar connection.

Fig. 6. Setup of the corrosion process for the slabs.

Table 3
Percentage of mass loss for the corroded slabs.

Group	Specimen ID	Duration of accelerated corrosion, day	Actual mass loss percentage, %	Theoretical mass loss percentage, % (faraday's equation)	Actual loss/Theoretical loss
Group I	S10	10	4	4	1
	S20	20	9	8	1.12
	S30	30	12	12	1
Group II	S10-EB−20	10	3	4	0.75
	S20-EB−20	20	8	8	1
	S30-EB−20	30	11.5	12	0.95
Group III	S10-NSE−20	10	2.5	4	0.625
	S20-NSE−20	20	6	8	0.75
	S30-NSE−20	30	11	12	0.91
Group IV	S10-NSE−35	10	2	4	0.5
	S20-NSE−35	20	5	8	0.625
	S30-NSE−35	30	10	12	0.83

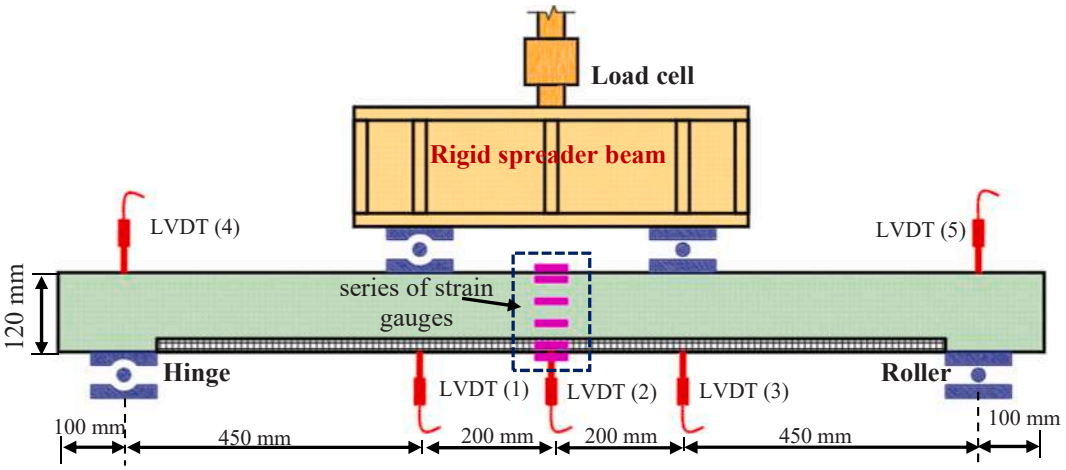


Fig. 7. Test setup and instrumentation.

current intensity increased sharply due to the loss of bond between the corroded bar and concrete. On the other hand, the strengthened slab showed almost a constant slope of the curve of current intensity which means a lower rate of corrosion. This confirms the ability of the SHCC to reduce the corrosion of the steel reinforcement compared to ordinary concrete.

3.2. Corrosion cracks and mass loss

Fig. 10 shows the corrosion cracks of the unstrengthened slabs of group I after 10, 20 and 30 days of corrosion exposure versus the strengthened slabs after 30 days of accelerated corrosion. As shown in the figure, the corroded slabs exhibited longitudinal cover cracking parallel to the internal steel bars. After the end of the corrosion process, the width of the developed cracks was measured using a digital microscope. For the un-strengthened slabs, after 10, 20 and 30 days of

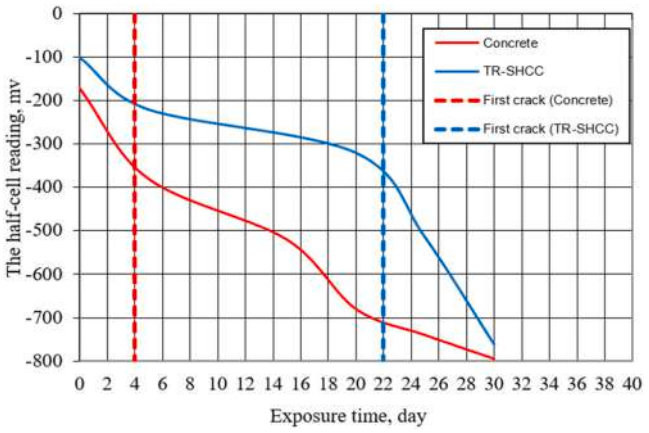


Fig. 8. The half-cell reading versus the exposure time.

accelerated corrosion, the crack width reached about 0.4, 0.6, and 0.9 mm, respectively. On the other hand, for the strengthened slab S30-NSE-35, the corrosion cracks appeared after 22 days, and the maximum crack width after 30 days was 0.05 mm. This value represents about 6 % of that achieved by the unstrengthened slab S30.

After the flexural loading tests, the slabs were demolished, and then the steel bars were extracted from the slabs. The bars were cut in pieces of 200 mm in length and then the rust products were removed according to ASTM G1–03–16 [49]. After removing the rust products, the bars were weighted to calculate the mass loss due to corrosion. Fig. 11 shows the distribution of the mass loss over the bar length. As shown in this figure, the highest value of the mass loss was at the middle of the bar and the value was decreasing by approaching the ends of the bars. Table 3 shows the maximum percentages of the mass losses of the main tensile steel. As shown in Table 3, the un-strengthened slabs recorded mass losses of 3, 9, and 12 % for durations of 10, 20, and 30 days of accelerated corrosion, respectively. On the other hand, the application of the strengthening decreased the lost mass. For group II, the mass losses were 4, 8, and 11.5 % for durations of 10, 20, and 30 days of accelerated corrosion, respectively. For the slabs of group III, the mass losses were 2.5, 5, and 11 % for durations of 10, 20, and 30 days of accelerated corrosion, respectively. For the slabs of group IV, the full surrounding of the tensile steel with the SHCC layer showed the lowest mass loss, the mass losses were 2, 6, and 10 % at 10, 20, and 30 days of accelerated corrosion, respectively. This reflects the ability of the SHCC material to reduce the steel corrosion.

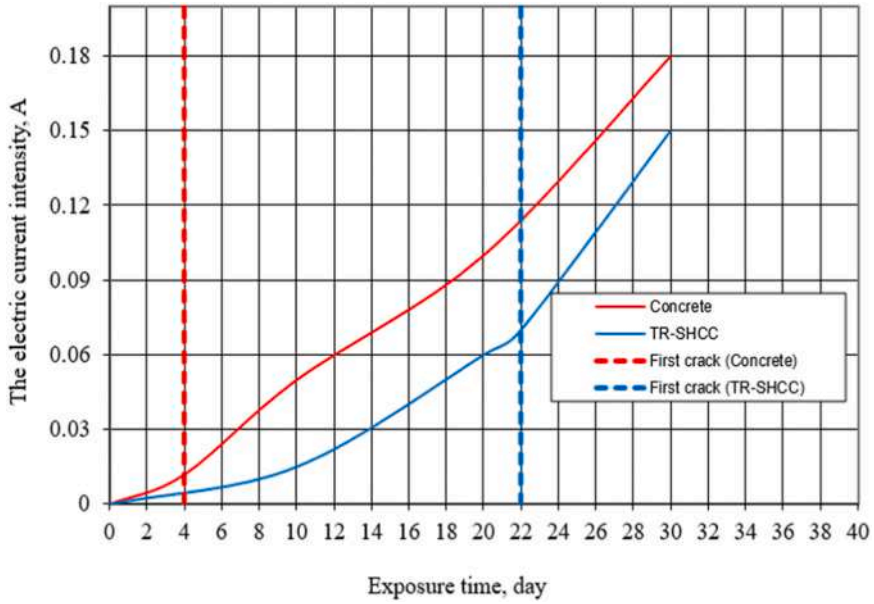
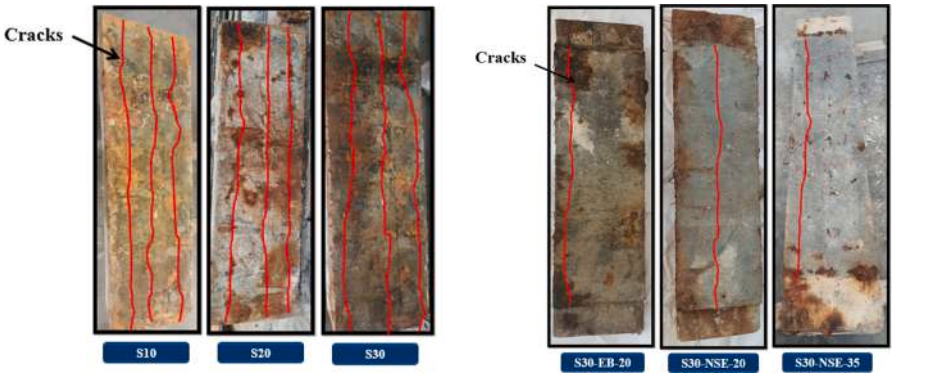


Fig. 9. The electric current intensity versus the exposure time.



(a) The unstrengthened slabs (b) The strengthened slabs after 30 days of corrosion

Fig. 10. Cracks at the bottom face of group I versus the strengthened after 30 days of accelerated corrosion.

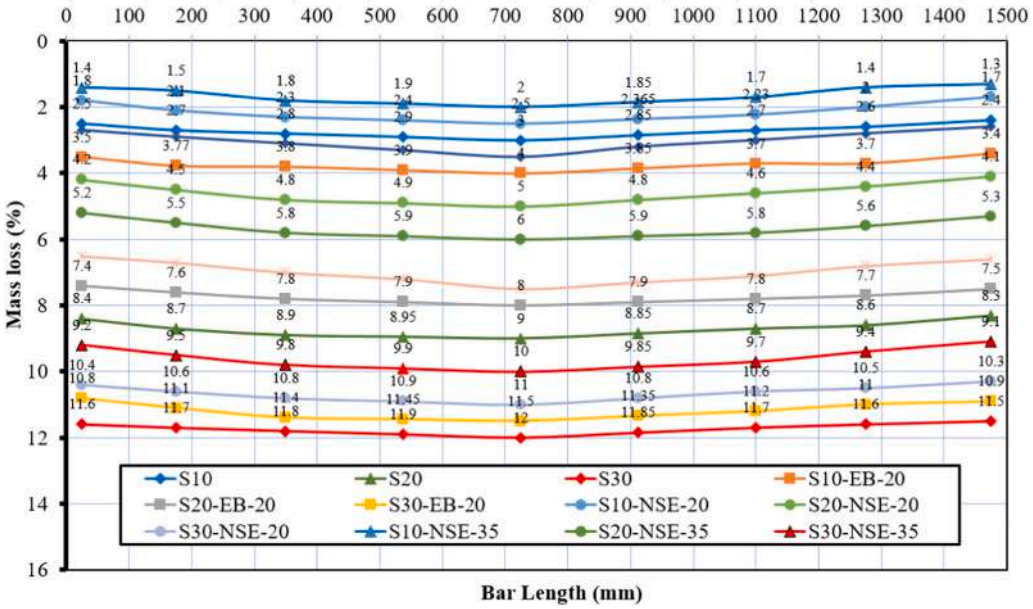


Fig. 11. Mass loss distribution.

3.3. Ultimate capacity and failure modes

Fig. 12 shows the final crack pattern of the slabs. Fig. 13, shows samples of the different failure modes of the slabs. The values of cracking, yielding and ultimate loads are listed in Table 4. Also, Figs. 14 and 15 plot relations between the ultimate loads versus the corrosion duration and the actual mass loss, respectively. For the uncorroded slab S0, the initial crack took place at the maximum moment zone of the slab at about 18 kN, following, more cracks were developed away from this zone and towards the supports. Reaching about 51.00 kN, slab S0 failed in flexural tension failure, as shown in Fig. 13a. The failure was governed by the yielding of tension reinforcement followed by concrete crushing at the compression zone. For the corroded slabs of group I, the slabs exhibited two distinguished failure modes, slabs S10 and S20 failed in a similar failure fashion to that of Slab S0 (flexural tension failure) with a reduction in the ultimate capacity by about 8 and 25 %, respectively. At failure, slab S20 exhibited concrete cover spalling, as shown in Fig. 12a. Whereas, for slab S30 (corrosion duration of 30 days), the first flexural crack took place at the mid-span at a load of 7.0 kN. With the load increase, diagonal cracks appeared in the shear span near the support and started to propagate with some inclination toward the loading points. Finally, slab S30 failed due to the splitting of the steel reinforcement, as shown in Fig. 13b. This is owing to the increase in the corrosion duration for 30 days which made a significant loss in the bond between the reinforcing bars and the surrounding concrete. The maximum ultimate load of S30 was 27 kN, which is about 53 % of slab S0.

Regarding group II (strengthened with EB TR-SHCC), as shown in Fig. 12, the slabs exhibited three different failure modes. For slab S0-EB-20, the first flexural crack took place in the TR-SHCC layer at about 25 kN, which is 39 % higher than S0. Increasing the applied load, the cracks extended to the concrete substrate and several micro-cracks appeared over the strengthening layer. At about 53.9 kN, the yielding of the internal reinforcement took place. After yielding, the width of the cracks increased considerably increased. Finally, at a load of 81 kN, the slab failed due to the textile rupture. Compared to the studied slabs, this was the highest load-carrying capacity. As for slabs S10-EB-20, and S20-EB-20 the first flexural crack took place at the mid-span in the TR-SHCC layer at loads of 23 and 22 kN, respectively. Following, the slabs exhibited a similar behavior to that of S0-EB-20 until the yielding of the steel bars. After yielding, slabs S10-EB-20, and S20-EB-20 failed due to the debonding of the strengthening from the concrete surface accompanied by peeling-off of the concrete cover, as shown in Fig. 13c. This is owing to the deterioration of the concrete cover due to corrosion. However, the obtained ultimate loads were higher than those of the unstrengthened slabs S10 and S20 by about 28 and 18 %, for slabs S10-EB-20 and S20-EB-20, respectively. The corrosion decreased the ultimate capacities of slabs S10-EB-20 and S20-EB-20 by about 26 and 44 %, compared to slab S0-EB-20. As for slab S20-EB-30, the slab exhibited similar behaviour to that of the unstrengthened slab S30, without almost any effect of the strengthening layer. The slab failed due to the splitting of the tension steel at a load of 29 kN (1.07 of that of S30).

As for group III, slabs S0-NSE-20 and S10-NSE-20 exhibited similar behaviour to slab S0-NSE-20. The first crack took place at the mid-span on the TR-SHCC layer at loads of 23 and 22 kN for slabs S0-NSE-20 and S10-NSE-20, respectively. Increasing the applied load, the cracks extended to the concrete substrate and several micro-cracks spread over the strengthening layer. After the yield of internal reinforcement, the slabs failed due to the textile rupture, followed by concrete crushing at the compression zone. For slabs S0-NSE-20 and S10-NSE-20, the ultimate loads were 76 and 70 kN, respectively. Comparing the test results of these slabs with their counterparts in group II, the EB strengthening technique achieved higher capacity with the uncorroded slab by about 6.5 %, however, the NSE technique with partial replacement of concrete cover by SHCC material was more efficient after corrosion exposure. For slab S10-NSE-20 (corrosion duration 20 days), the achieved ultimate load was 16 % higher than slab S10-EB-20 ($P_u = 60$ kN). For slabs S20-NSE-20 and S30-NSE-20, increasing the duration of corrosion to 20 and 30 days, changed the failure mode of the slabs and reduced the efficiency of the strengthening. The slabs failed due to the debonding of the strengthening from the concrete surface. For S20-NSE-20 and S30-NSE-20, the ultimate loads were 55 and 36 kN, respectively. Nevertheless, these values are higher than slabs S20-EB-20 and S30-EB-20 by about 22 and 24 %, respectively.

Regarding the slabs of group IV, all the uncorroded and corroded slabs exhibited similar cracking patterns and failure modes to those achieved by the uncorroded slabs S0-EB-20 and S0-NSE-20. In addition, at the ultimate load, the slabs of group IV failed due to the textile rupture without any sign of debonding between the strengthening layer and the concrete substrate, as shown in Fig. 13d. The ultimate loads of slabs S0-NSE-35, S10-NSE-35, S20-NSE-35 and S30-NSE-35 were 80, 77, 72 and

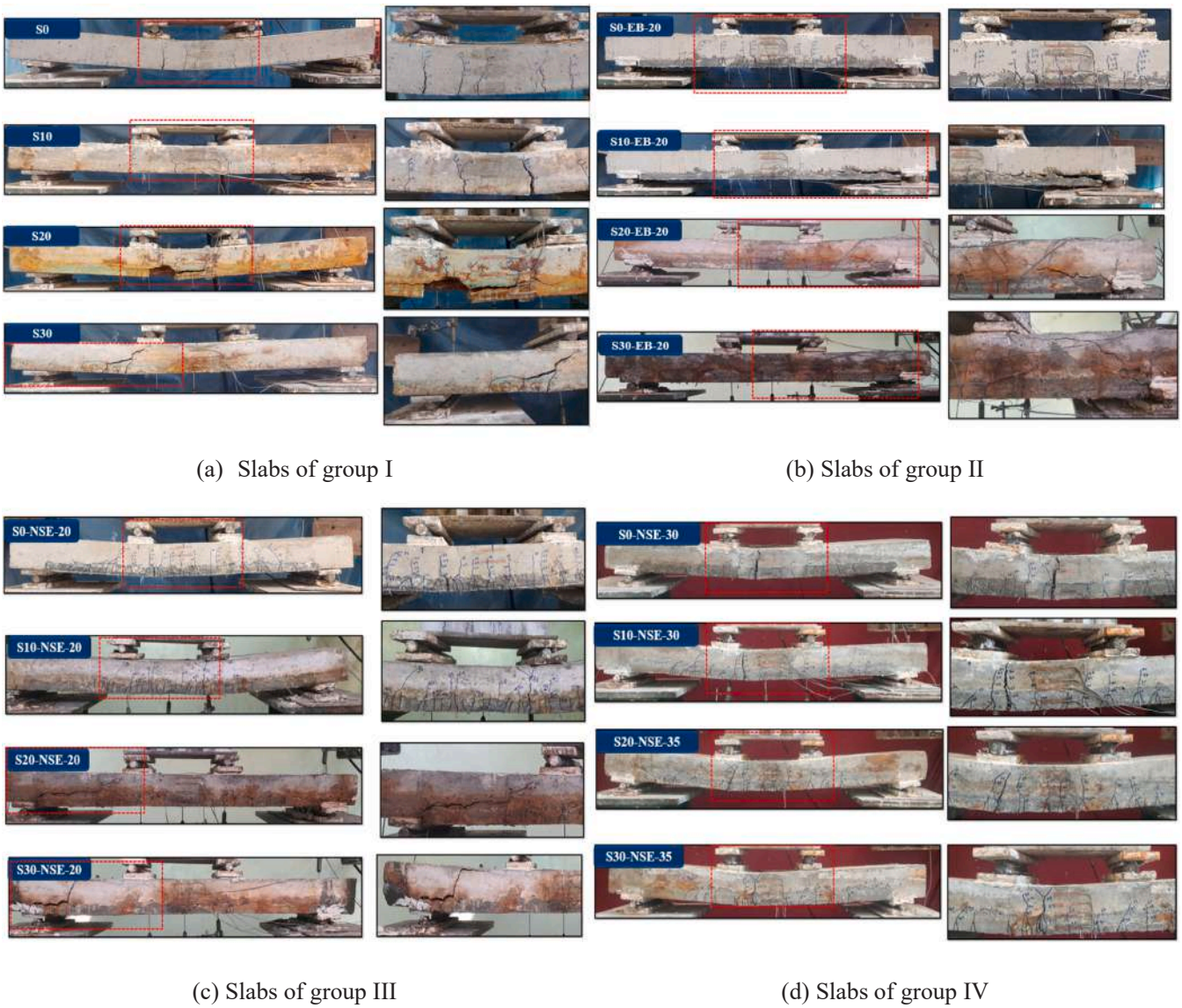


Fig. 12. Final crack pattern of the tested slabs.

65 kN, respectively. These loads are about 5, 10, 31 and 80 % higher than those of slabs S0-NSE-20, S10-NSE-20, S20-NSE-20 and S30-NSE-20, respectively. It can be concluded that replacing the concrete cover with SHCC material before the application of the TR-SHCC could effectively preclude the loss of the strengthening efficiency, especially when the SHCC is fully coating the tension steel reinforcement.

3.4. Load-deflection response and ductility

The load versus deflection curves of the slabs are shown in Fig. 16. Also, Table 4 lists the values of deflections corresponding to cracking, yielding, and ultimate loads. As shown in Fig. 16a, the load versus deflection curve of the uncorroded slab S0 can be categorized into three primary stages. The initial stage begins from zero load until the initial crack appears. Afterward, the second stage begins from the first crack load until the yielding of the steel bars. In the second stage, a considerable decrease in the slope of the load-deflection curve was noticed. In the third stage, after yielding of the steel reinforcement, the slab showed a plastic deformation without further increase in the applied load until concrete crushing. The maximum deflection of slab S0 was 49.32 mm. As for the remaining slabs of group I, the corrosion had a significant effect on the behaviour of the unstrengthened slabs. However, slabs S10 and S20 showed almost similar load-deflection response to that of S0, the corrosion decreased the slabs' stiffness and increased the deflection at the same load. At ultimate, the maximum deflections of slabs S10 and S20 were 36.31 and 26.41 mm, respectively. As for slab S30, before the yielding of the steel bars, a sudden drop in the load and a great decrease in the ultimate deflection were noticed. The value of the ultimate deflection of slab S30 was 7.93 mm, which is 16 % of that of slab S0.

For the strengthened uncorroded slab S0-EB-20, the load-deflection curve is categorized into four primary stages. The first and second stages were similar to slab S0, however, the un-strengthened slab showed higher stiffness. In the third stage, after yielding of the internal reinforcement, the slab behaved a deflection hardening behaviour till the textile rupture. The rupture of the textile caused a sudden reduction in the load capacity. In the fourth stage, the load decreased to a level close to the yielding load, and the slab behaved a plastic deflection until concrete crushing. The maximum achieved deflection of slab S0-EB-20 was 18.17 mm. As for the corroded slabs of group II, as shown in Fig. 16a, the corrosion had a significant effect on the behaviour of the EB-strengthened slabs. Increasing the corrosion duration decreased the slab stiffens and then increased the developed defection. Moreover, the slabs failed suddenly before the rupture of the textile reinforcement with a great reduction in the ultimate deflection. For slabs S10-EB-20, S20-

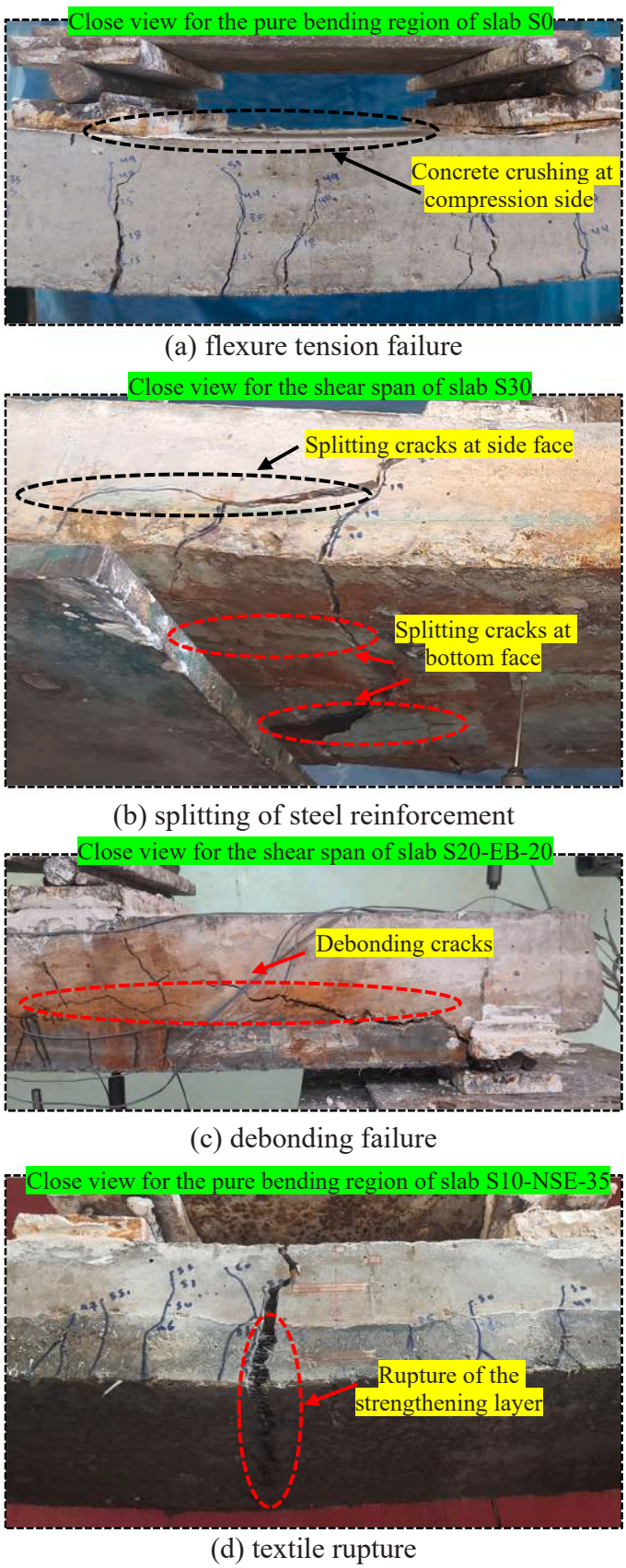


Fig. 13. Different failure modes of the tested slabs.

EB-20 and S30-EB-20 the ultimate deflections were 10.5, 6.30 and 4.06 mm, respectively. These values are about 60, 36 and 23 % of that achieved by slab S0-EB-20, respectively.

Regarding group III, as shown in Fig. 16b, the uncorroded slab S0-NSE-20 and the corroded slab S10-NSE-20 showed a similar trend to that of the uncorroded slab S0-EB-20, unless slab S0-EB-20 showed higher stiffens and lower deflection values, at the same load level. At ultimate, slabs S0-NSE-20 and S10-NSE-20 demonstrated rupture of textile reinforcement and achieved ultimate deflections of 17.47 and 16.5 mm, respectively. On the other hand, increasing the corrosion exposure to 20 and 30 days for slabs S20-NSE-20 and S30-NSE-20, respectively, led to a sudden debonding failure accompanied by a decrease in the ultimate deflection. The values of the ultimate deflection of slabs S20-NSE-20 and S30-NSE-20 were 9.6 and 5.21 mm, respectively. These values are about 55 and 30 % of that achieved by slab S0-NSE-20, respectively.

Figs. 16c and 16d show comparisons between the slabs of group IV and those of groups II and III. As shown in these figures, the corroded slabs of group IV showed a similar trend to that of the strengthened uncorroded slabs. Before the failure, the corroded slabs reached the rupture of the textile reinforcement with a good improvement in the ultimate deflection compared to their counterparts in groups II and III. The values of the ultimate deflections of slabs S10-NSE-35, S20-NSE-35 and S30-NSE-35 were 18.40, 16.64 and 15.31 mm, respectively. These values are about 75, 164 and 277 % higher than those achieved by their counterpart slabs in group II.

The deflection-based ductility index (μ) is the ratio of the deflection at ultimate load (Δ_u) to that at yield load (Δ_y) [50]. Table 4 shows the values of ductility indices for the slabs. As shown in Table 4, slab S0 achieved the highest ductility index of 5.62. In general, compared to the uncorroded slabs, the corroded slabs achieved lower values of ductility indices. For instance, for slabs S10, S20 and S30, the values of ductility indices were 4.73, 3.45 and 1.16, respectively. These values are about 35, 53, and 84 %, respectively, of that obtained by slab S0. Comparing the obtained results of the strengthened slabs, before exposure to corrosion, the strengthened slab S0-EB-20 showed the highest ductility index compared to the other strengthened slabs. However, after corrosion exposure, the strengthened slabs of group IV showed the best performance compared to the others corroded in groups II and III. For instance, the ductility indices for slabs S10-NSE-35 and S20-NSE-35 were 2.45 and 2.24, respectively. These values are 45 and 121 % higher than slabs S10-EB-20 and S20-EB-20, respectively.

The absorbed energy (E) is defined as the integration of the area below the load deflection curve up to the ultimate load [51]. Table 4 shows the calculated absorbed energies for the slabs. Similar to the trend of the ductility index, the corrosion decreased the absorbed energy of the slabs. For instance, the absorbed energy for the control slab was 2379 kN.mm. Whereas, for slabs S10, S20 and S30, the absorbed energies were 1500, 927, and 243 kN.mm, respectively. Also, compared to the strengthened slabs, slab S0-EB-20 showed the highest value of absorbed energy. The absorbed energy for slab S0-EB-20 was 1135 kN.mm. On the other hand, the corroded slabs of group IV showed better values of absorbed energies than the other strengthened corroded slabs. For instance, the absorbed energies for slabs S10-NSE-35, S20-NSE-35, and S30-NSE-35 were 1008, 847 and 708 kN.mm, respectively. On the other hand, the absorbed energies for slabs S10-EB-20, S20-EB-20, and S30-EB-20 were 444, 186 and 119 kN.mm, respectively.

3.5. Load-crack width response

The crack width plays a key role in the durability of the RC structures, especially in severe environmental conditions. Thus, the design codes set a conservative limit for the maximum crack width ($W_{k,max}$) in such cases. Under ordinary conditions, at service load level, both ACI-318 [52] and ECP-203 [53] set a limit of 0.3 mm for the maximum permissible crack width, while, under severe and aggressive

Table 4
Summary of test results.

Group	Specimen ID	At first flexural cracks		At service load			At yield load		At ultimate load			μ	E, kN.mm	Mode of failure
		P, mm	Δ, mm	P, kN	W_k, mm	$W_k/W_{k,max}$	P, kN	Δ, mm	P, kN	Δ, mm	W_k, mm			
Group I	S0	18	1.71	34	0.09	0.9	45	8.77	51	49.32	2.40	5.62	2379	Flexural tension failure
	S10	15	1.32	31	0.15	1.5	41	9.11	47	36.31	4.00	3.98	1500	Flexural tension failure
	S20	9.5	1.36	25	0.22	2.2	37	9.38	38	26.41	4.20	2.81	927	Flexural tension failure
	S30	7.0	1.19	18	0.30	3.0	-	-	27	7.93	4.41	-	243	Splitting of the steel reinforcement
Group II	S0-EB−20	25	1.05	54	0.07	0.7	61	6.65	81	18.17	1.49	2.73	1135	Textile rupture
	S10-EB−20	23	1.5	40	0.14	1.4	52	6.25	60	10.50	1.64	1.68	444	Debonding with peeling off of the concrete cover
	S20-EB−20	22	1.7	30	0.16	1.6	46	6.23	45	6.30	1.80	1.01	186	Debonding with peeling off of the concrete cover
	S30-EB−20	21	2	19	0.20	2.0	-	-	29	4.06	1.98	-	119	Splitting of the steel reinforcement
Group III	S0-NSE−20	23	1.2	51	0.08	0.8	58	7.29	76	17.47	1.65	2.39	958	Textile rupture
	S10-NSE−20	22	1.38	47	0.12	1.2	49	7.40	70	16.50	1.74	2.22	817	Textile rupture
	S20-NSE−20	21	1.51	37	0.13	1.3	42	7.46	55	9.60	1.91	1.28	467	Debonding of the strengthening
	S30-NSE−20	20	1.9	24	0.14	1.4	-	-	36	5.21	2.10	-	119	Debonding of the strengthening
Group IV	S0-NSE−35	24	1.3	53	0.07	0.7	60	7.67	80	19.30	1.50	2.51	1118	Textile rupture
	S10-NSE−35	23	1.5	51	0.08	0.8	58	7.50	77	18.40	1.58	2.45	1008	Textile rupture
	S20-NSE−35	22	1.6	48	0.09	0.9	56	7.41	72	16.64	1.66	2.24	847	Textile rupture
	S30-NSE−35	21	1.65	43	0.09	0.9	54	7.39	65	15.34	1.74	2.07	708	Textile rupture

P = load; Δ= deflection, W_k = major flexural crack width; $W_{k,max}$ = maximum crack width according ACI-318 and ECP-203, μ = ductility factor; *E* = absorbed energy

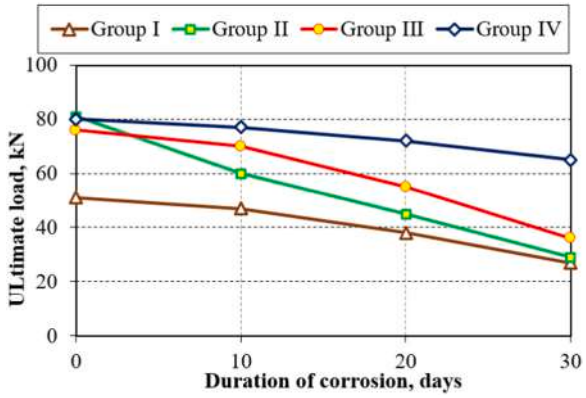


Fig. 14. Relation between ultimate load and corrosion duration.

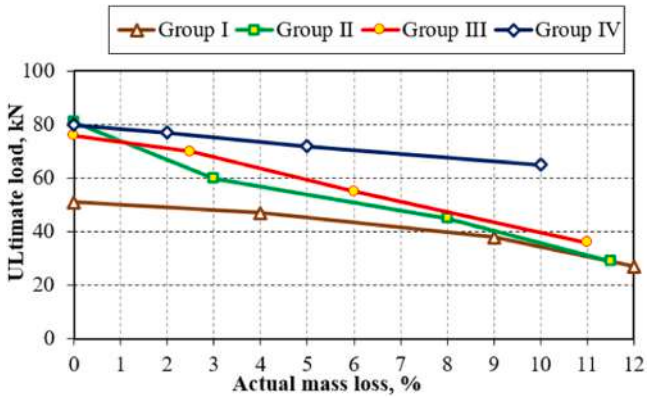


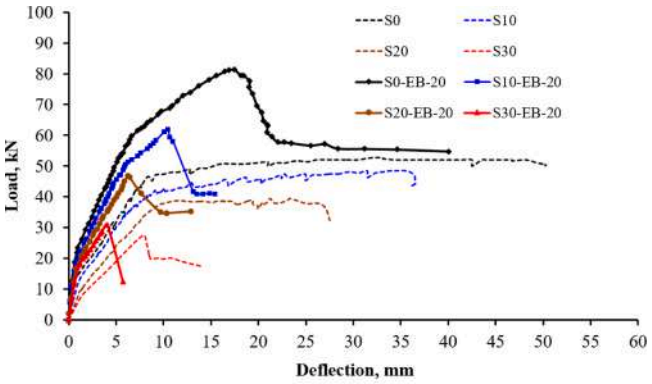
Fig. 15. Relation between ultimate load and actual mass loss.

environments, the limiting value was reduced to 0.1 mm. The load-crack width curves of the slabs are shown in Fig. 17. Also, Table 4 summarizes the measured crack width corresponding to the service load of each slab. As shown in Fig. 17a, the corroded slabs of group I showed higher values of crack widths compared to slab S0. Moreover, at the service load, the maximum crack width of slab S0 was 0.09 mm, while, for slabs S10, S20 and S30 the maximum crack widths were 0.15, 0.22 and 0.30 mm, respectively, which exceed the limiting value by about 50, 120 and 200 %, respectively. The increase in the crack width of the corroded slabs is a result of both the decrease in the bond between the steel reinforcement and the surrounding concrete and the decrease in the tension stiffness due to the mass loss of the steel reinforcement. For group II, as shown in Fig. 17, despite the application of the externally bonded TR-SHCC decreased the value of crack width compared to the corroded slabs of group I, at the service load, the crack width of the corroded slabs exceeded the limiting value by about 40, 60 and 100 % for slabs S10-EB-20, S20-EB-20 and S30-EB-20, respectively.

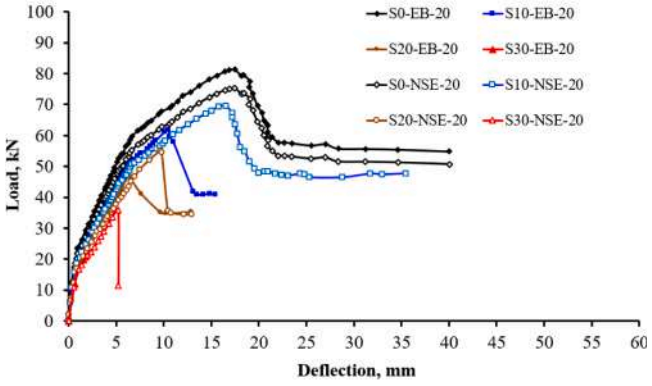
Regarding the strengthened slabs, the near-surface embedded technique decreased the value of the measured crack width, especially with group IV, when the SHCC layer was coating the steel reinforcement. As shown in Fig. 17, group IV showed the best improvement in crack width results after the corrosion exposure. As shown in Table 4, at the service load, the maximum crack width in group IV did not reach the limiting value. For slabs S0-NSE-35, S10-NSE-35, S20-NSE-35 and S30-NSE-35 the maximum crack width values at service load were 0.07, 0.08, 0.09 and 0.09 mm, respectively. This improvement in crack width results of group IV is owing to the crack-bridging action and multiple-cracking of the SHCC, in addition to, the higher interfacial bond between the steel bars and the SHCC material.

3.6. Strain results

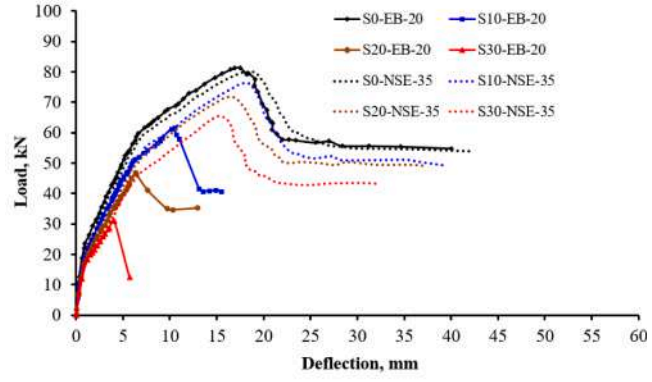
The curves of load versus steel strain of the slabs are shown in Fig. 18. Also, Fig. 19 shows the curves of load versus CFRP strain of the strengthened. As per the carried-out tests on the steel bars, the measured yield strain was 2500 με. Fig. 20 shows the strain distributions across the depth at the mid-span point of the slabs. The strain distributions across



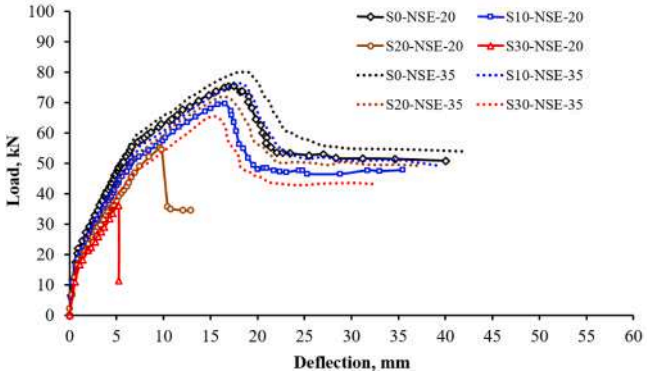
(a) groups I and II



(b) groups II and III

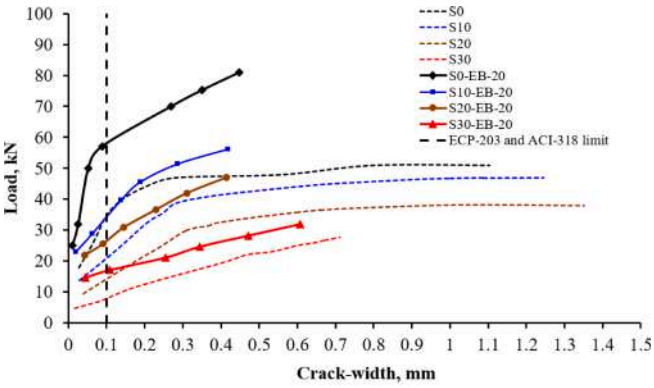


(c) groups II and IV.

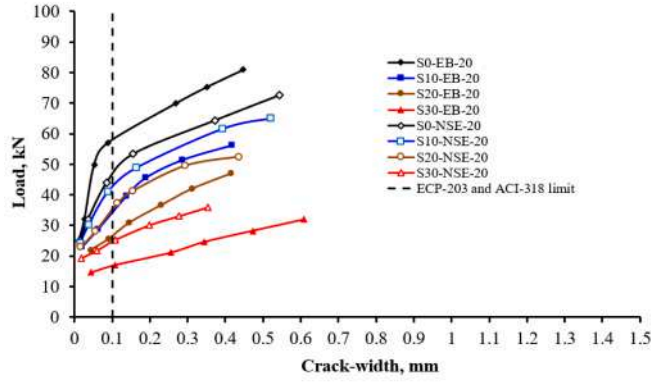


(d) groups III and IV.

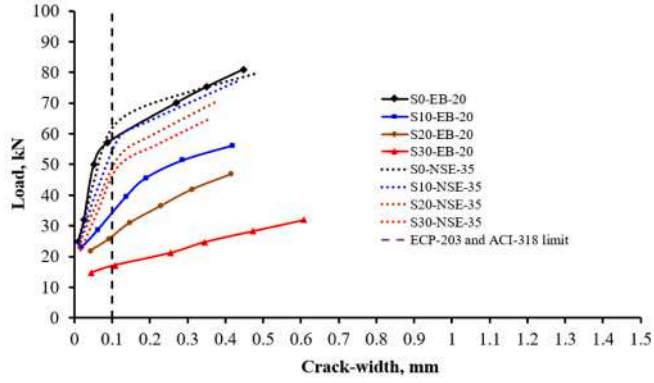
Fig. 16. Load deflection curves of the tested slabs.



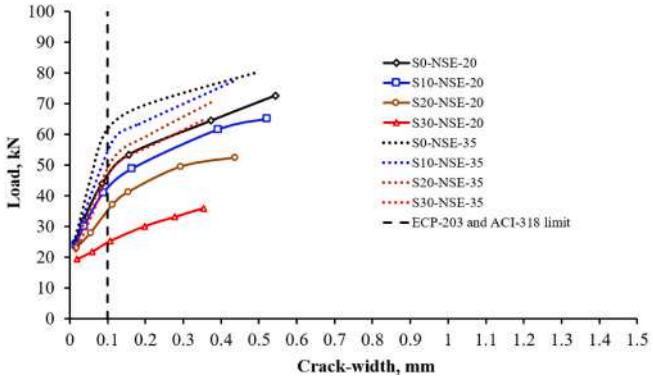
(a) groups I and II



(b) groups II and III

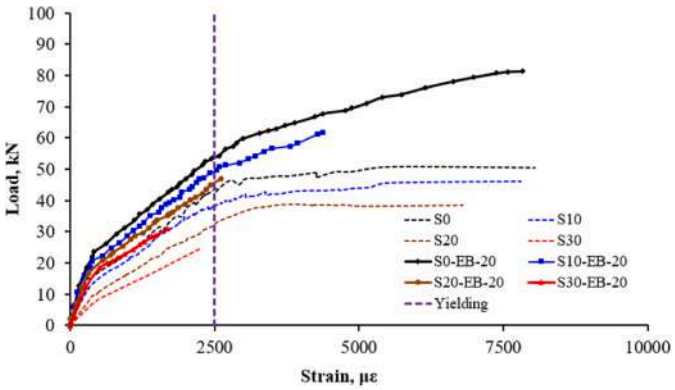


(c) groups II and IV

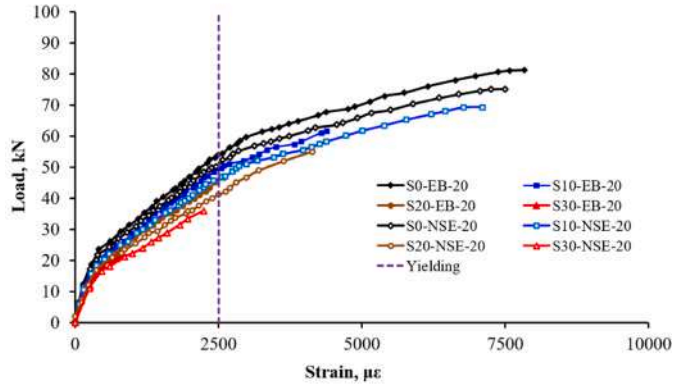


(d) groups III and IV

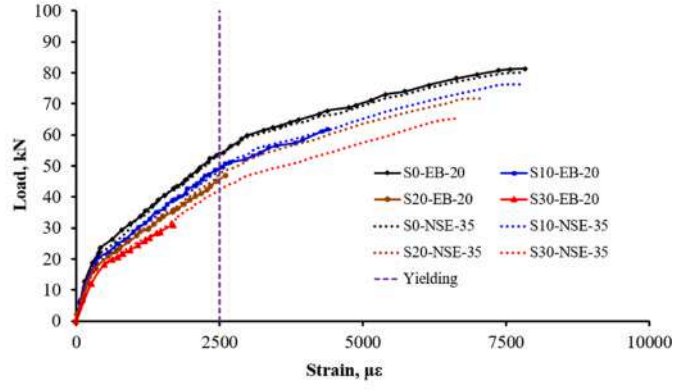
Fig. 17. Load-crack width curves for the tested slabs.



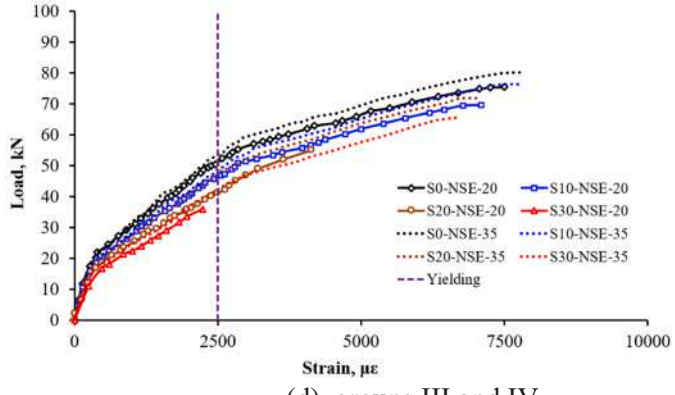
(a) groups I and II



(b) groups II and III

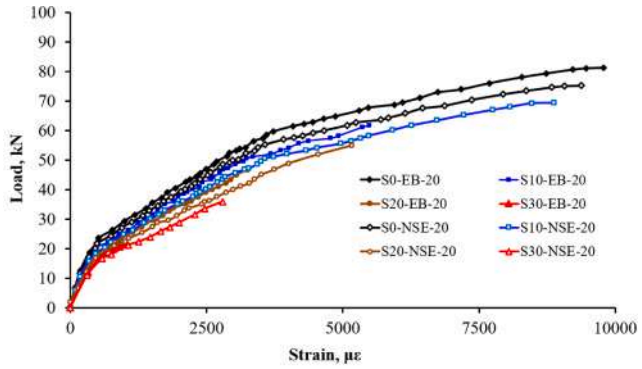


(c) groups II and IV

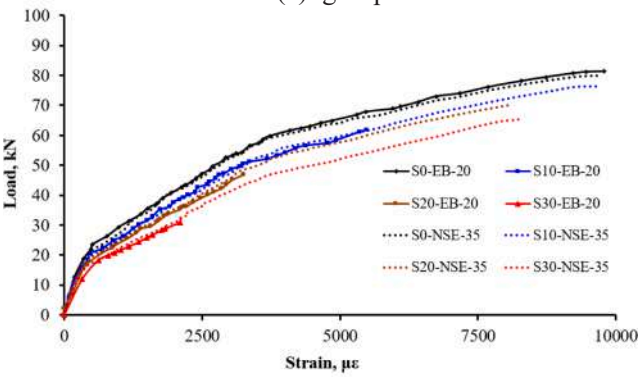


(d) groups III and IV

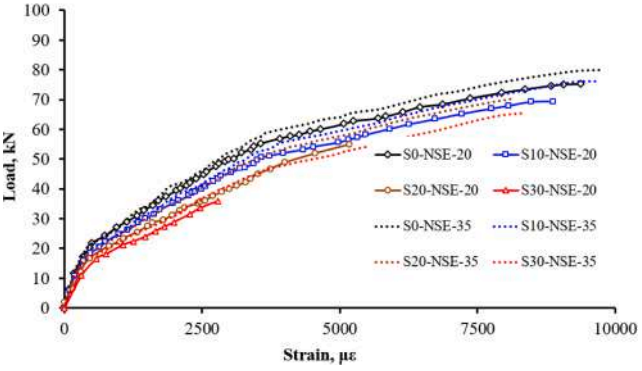
Fig. 18. Load-steel strain curves for the tested slabs.



(a) groups II and III



(b) groups II and IV



(c) groups III and IV

Fig. 19. Load CFRP strain for the tested slabs.

the depth of the mid-span section of the slabs are plotted at the cracking load, 0.35 P_u, 0.70 P_u, and the ultimate load (P_u). The strain results confirmed the obtained modes of failures; (1) except slab S30, the yielding of the internal steel reinforcement was observed in all slabs before failure, (2) As shown in Fig. 20, for slabs S0-EB-20, S0-NSE-20, S10-NSE-20 and the slabs of group IV, the strain distribution was linear at all stages of loading, which assures the full bond between the SHCC and the concrete substrate. On the other hand, slabs S10-EB-20, S20-EB-20, S20-NSE-20 and S30-NSE-20 showed a sudden change in the slope of the stain distribution at ultimate due to the debonding failure.

4. Analytical formulations

In the current study, two modes of failures were obtained for the TR-SHCC strengthened slabs after corrosion exposure. The first failure mode was a rupture of the CFRP textile followed by concrete crushing at the compression zone. The second mode was a debonding failure between the strengthening layer and the concrete substrate before the CFRP rupture. In this section, the analytical study was limited only to the slabs

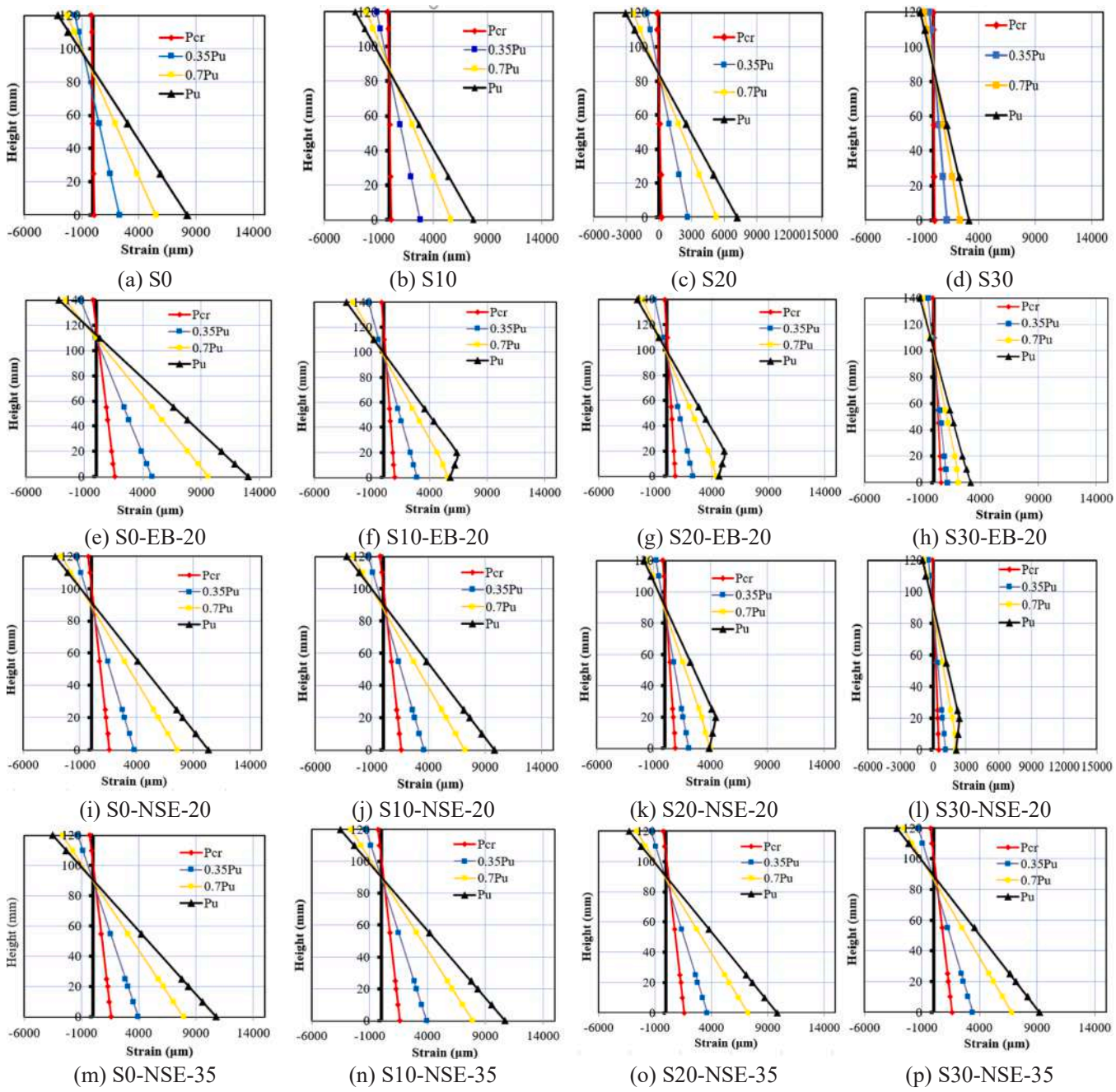


Fig. 20. Strain distribution for the tested slabs.

that failed after the rupture of CFRP, at which the debonding of the strengthening layer did not occur and the strain compatibility approach could then be applied. Based on the stress and strain distributions shown in Fig. 21, sectional analysis was conducted to calculate the ultimate moment of TR-SHCC-strengthened corroded slabs. For the prediction of the flexural moment, the following assumptions were considered:

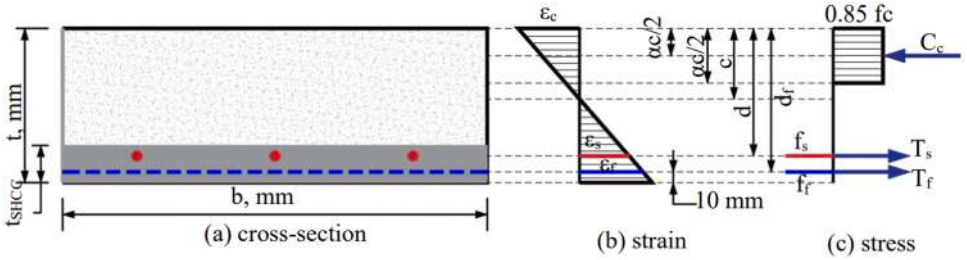


Fig. 21. Strains and stresses of a section strengthened with TR-SHCC.

- Following ACI-318 [52], the concrete compressive strain (ε_c) at ultimate equals 0.003, because the concrete crushing occurred.
- At the ultimate stage, the contribution of concrete at the tension zone was neglected [52].
- Following JSCE recommendations [45], since the SHCC material has improved the tensile strength, the contribution of the SHCC material at the tension side was considered.

- Based on the experimental observations, a perfect bond between the FRP textile and SHCC material was considered.
- Based on the equations proposed by Du et al. [50], the reduced yield strength (f_{yc}) and cross-sectional area (A_{sc}) of the corroded steel bars were determined. Du et al. suggested the following equations, which are derived in terms of the actual mass loss of the steel bars.

$$f_{yc} = 0.005(200 - X_p)f_y \tag{2}$$

$$A_{SC} = 0.01(100 - X_P)A_s \tag{3}$$

Where

f_y = yield strength of the steel reinforcement; A_s = the original area of the steel bars before corrosion; X_p = the actual mass loss of the bars after corrosion.

- At failure, the rupture of FRP textile took place, thus the effective tensile stress in the FRP textile (f_{fe}) was obtained based on the following equation:

$$f_{fe} = E_f \times \varepsilon_{fe} \tag{4}$$

$$\varepsilon_{fe} = \varepsilon_{fd} \leq 0.012 \tag{5}$$

Where

ε_{fe} = effective tensile strain of the FRP textile at failure; ε_{fd} = the design tensile strain.

Following the previous assumptions, the ultimate flexural moment (M_u) of the TR-SHCC strengthened corroded slabs could be obtained as follows:

$$M_u = T_s \ (d - \beta \times 0.5c) + T_f \ (d_f - \beta \times 0.5c) \tag{6}$$

Where

$$T_s = A_{sc} \times f_{yc} \tag{7}$$

$$T_f = A_f \times n \times w_f \times f_{fe} + A_{SHCC} \times f_{y,SHCC} \tag{8}$$

The height of the compression zone (c) can be calculated as follows:

$$c = \frac{A_{sc} \times f_{yc} + A_f \times n \times w_f \times f_{fe} + A_{SHCC} \times f_{y,SHCC}}{\alpha \times \beta f_c' \times b} \tag{9}$$

Where

A_f = area of mesh reinforcement by unit width (in the current study $A_f = 0.0275\ mm^2/mm$); w_f = width of the CFRP textile strip (in the current study $w_f = 375$ mm); n = Number of the CFRP textile layers (in the current study n = 1); A_{SHCC} = cross-sectional area of the SHCC layer; f_c' = concrete compressive strength; $f_{y,shcc}$ = the first cracking strength according to JSCE recommendations [36]; b = the width of the slab; d = the depth of the slab; α and β = the factors of stress block.

The factors of concrete stress block (β *and* α) and the modulus of elasticity of concrete (E_c) were obtained by the following equations:

$$E_c = 4700\sqrt{f_c'} \tag{10}$$

$$\varepsilon_c' = \frac{1.7 \ f_c'}{E_c} \tag{11}$$

$$\beta = \frac{4\varepsilon_c' - \varepsilon_c}{6\varepsilon_c' - \varepsilon_c} \tag{12}$$

$$\alpha = \frac{3\varepsilon_c'\varepsilon_c - \varepsilon_c^2}{3\beta - \varepsilon_c'^2} \tag{13}$$

A comparison between the experimental and the predicted ultimate moments is presented in Table 5. As shown in the Table, the proposed flexural strength model gave a good prediction for the ultimate moment. The average value (mean) of the experimental to predicted moments ($M_{u,\ exp}/M_{u,\ p}$) was 0.99 and the coefficient of variation (*COV*) was 0.002.

5. Conclusion

This study evaluated the flexural behavior of three different regimes of TR-SHCC strengthening after accelerated corrosion exposure. The strengthening regimes were: (1) the application of an EB layer without removing the concrete cover; (2) the application of a NSE layer after partial SHCC-replaced concrete cover; and (3) the application of a NSE layer with full SHCC-replaced cover. After strengthening the slabs were subjected to different durations of accelerated corrosion. After the end of the corrosion process, the slabs were tested under a four-point bending scheme. Based on the results of the experimental and analytical investigations the following conclusion could be drawn:

- Compared with the studied slabs, the EB-TR-SHCC strengthening recorded the highest load-carrying capacity before the corrosion exposure. However, after the corrosion exposure, the EB-strengthened slabs failed in either debonding between the strengthening layer or tension steel splitting recording the highest reduction in the load-carrying capacity compared to the other strengthening techniques. Moreover, after 30 days of accelerated corrosion, the strengthening showed an insignificant effect on the slab behaviour.
- After corrosion exposure, the NSE-TR-SHCC strengthening with partial SHCC-replaced cover was more efficient than the EB-strengthening. However, increasing the corrosion exposure to more than 20 days, changed the failure mode of the slabs from textile rupture to a debonding failure between the strengthening layer and the substrate concrete and decreased the strengthening efficiency.
- Compared to the other corroded slabs, the NSE-TR-SHCC strengthening with full SHCC-replaced cover (the SHCC coating the steel bars) achieved the highest strengthening efficiency. All the corroded slabs failed due to a rupture of the textile followed by concrete crushing without any sign of debonding between the strengthening layer and the concrete substrate at failure.
- The NSE-TR-SHCC strengthened slabs with full SHCC-replaced concrete cover showed the best improvement in crack width results after

Table 5
Comparison between the experimental and predicted results.

Specimen ID	P_u, kN	$M_{u,exp}$, kN.m	$M_{u,P}$, kN.m	$M_{u,exp}/M_{u,P}$
S0	51	11.47	10.57	1.08
S10	47	10.57	10.01	1.05
S20	38	8.55	9.22	0.93
S0-EB−20	81	18.22	18.18	1.00
S0-NSE−20	76	17.10	17.01	1.01
S10-NSE−20	70	15.75	16.09	0.98
S0-NSE−35	85	19.12	18.61	1.03
S10-NSE−35	82	18.45	18.34	1.01
S20-NSE−35	77	17.32	17.91	0.97
S30-NSE−35	70	15.75	17.23	0.917
			Mean	0.99
			SD	0.049
			COV	0.002

P_u = experimental ultimate load; $M_{u,exp}$ = experimental ultimate moment = 0.225 P_u; $M_{u,P}$ = predicted ultimate moment.

the corrosion exposure. At the service load, contrary to the other strengthening regimes, the maximum crack width of the slabs did not reach the codes limits.
- The NSE-TR-SHCC strengthened slabs with full SHCC-replaced concrete cover showed higher ductility indices and absorbed energies than the other strengthened corroded slabs.
- The proposed flexural strength model gave good results for the ultimate moment of the TR-SHCC-strengthened corroded slabs. The average value of the experimental to predicted moments and the coefficient of variation were about 0.99 and 0.002, respectively.

This work guides for a better selection of a reliable strengthening system for the RC slabs that are expected to be susceptible to corrosion attack. It could be noted that the proposed strengthening can be used for beams and columns, which are vulnerable to corrosion. In future work, the long-term performance of the strengthening systems is suggested to be evaluated.

CRediT authorship contribution statement

Mahmoud Mohamed H.: Supervision, Conceptualization. **El-Shafiey Tarek F.:** Supervision. **Khaled Essam:** Writing – original draft, Methodology, Investigation, Data curation. **Hassan Ali:** Writing – review & editing, Writing – original draft, Supervision, Resources, Methodology, Investigation, Formal analysis, Data curation, Conceptualization.

Declaration of Competing Interest

The authors declare that they have no known competing financial interests or personal relationships that could have appeared to influence the work reported in this paper.

Data availability

Data will be made available on request.

References

[1] Park J, Hong S, Park SK. Experimental study on flexural behavior of TRM-strengthened RC beam: various types of textile-reinforced mortar with non-impregnated textile. Appl Sci 2019;9. https://doi.org/10.3390/app9101981.
[2] De Lorenzis L, Teng JG. Near-surface mounted FRP reinforcement: an emerging technique for strengthening structures. Compos Part B: Eng 2007;38(2):119–43. https://doi.org/10.1016/j.compositesb.2006.08.003.
[3] De Santis S, De Felice G. Tensile behaviour of mortar-based composites for externally bonded reinforcement systems. Compos Part B: Eng 2015;68:401–13. https://doi.org/10.1016/j.compositesb.2014.09.011.
[4] Koutas L, Pityzogia A, Triantafillou TC, Bousias SN. Strengthening of infilled reinforced concrete frames with TRM: study on the development and testing of textile-based anchors. J Compos Constr 2014;18:1–12. https://doi.org/10.1061/(asce)cc.1943-5614.0000390.
[5] Sneed LH, Verre S, Carloni C, Ombres L. Flexural behavior of RC beams strengthened with steel-FRCM composite. Eng Struct 2016;127:686–99. https://doi.org/10.1016/j.engstruct.2016.09.006.
[6] Elghazy M, El Refai A, Ebead U, Nanni A. Fatigue and monotonic behaviors of corrosion-damaged reinforced concrete beams strengthened with FRCM composites. J Compos Constr 2018;22:04018040. https://doi.org/10.1061/(asce)cc.1943-5614.0000875.
[7] Bencardino F, Carloni C, Condello A, Focacci F, Napoli A, Realfonzo R. Flexural behaviour of RC members strengthened with FRCM: state-of-the-art and predictive formulas. Compos Part B 2018;148:132–48. https://doi.org/10.1016/j.compositesb.2018.04.051.
[8] Aljazaeri ZR, Janke MA, Myers JJ. A novel and effective anchorage system for enhancing the flexural capacity of RC beams strengthened with FRCM composites. Compos Struct 2019;210:20–8. https://doi.org/10.1016/j.compstruct.2018.10.110.
[9] Sneed LH, D'Antino T, Carloni C, Pellegrino C. A comparison of the bond behavior of PBO-FRCM composites determined by double-lap and single-lap shear tests. Cem Concr Compos 2015;64:37–48. https://doi.org/10.1016/j.cemconcomp.2015.07.007.
[10] Koutas LN, Tetta Z, Bournas DA, Triantafillou TC. Strengthening of concrete structures with textile reinforced mortars: state-of-the-art review. J Compos Constr 2019;23(1):03118001. https://doi.org/10.1061/(ASCE)CC.1943-5614.0000882.
[11] Tetta ZC, Bournas DA. TRM vs FRP jacketing in shear strengthening of concrete members subjected to high temperatures. Compos Part B 2016;106:190–205. https://doi.org/10.1016/j.compositesb.2016.09.026.
[12] Li VC. On engineered cementitious composites (ECC) a review of the material and its applications. J Adv Concr Technol 2003;1. https://doi.org/10.3151/jact.1.215.
[13] Mündecke E, Mechtcherine V. Tensile behaviour of strain-hardening cement-based composites (SHCC) with steel reinforcing bars. Cem Concr Compos 2020;105. https://doi.org/10.1016/j.cemconcomp.2019.103423.
[14] Li M, Li VC. Cracking and healing of engineered cementitious composites under chloride environment. Acids Mater J 2011;108(3):333. ⟨http://hdl.handle.net/2027.42/94199⟩.
[15] Zhang Z, Zhang Q. Matrix tailoring of engineered cementitious composites (ECC) with non-oil-coated, low tensile strength PVA fiber. Constr Build Mater 2018;161:420–31. https://doi.org/10.1016/j.conbuildmat.2017.11.072.
[16] Xu LY, Huang BT, Li VC, Dai JG. High-strength high-ductility engineered/strain-hardening cementitious composites (ECC/SHCC) incorporating geopolymer fine aggregates. Cem Concr Compos 2022;125:104296. https://doi.org/10.1016/j.cemconcomp.2021.104296.
[17] Huang BT, Zhu JX, Weng KF, Li VC, Dai JG. Ultra-high-strength engineered/strain-hardening cementitious composites (ECC/SHCC): material design and effect of fiber hybridization. Cem Concr Compos 2022;129:104464. https://doi.org/10.1016/j.cemconcomp.2022.104464.
[18] Li VC, Wu C, Wang S, Ogawa A, Saito T. Interface tailoring for strain-hardening polyvinyl alcohol-engineered cementitious composite (PVA-ECC). Mater J 2002;99(5):463–72.
[19] Hassan A, Baraghith AT, Atta AM, El-Shafiey TF. Retrofitting of shear-damaged RC T-beams using U-shaped SHCC jacket. Eng Struct 2021;245. https://doi.org/10.1016/j.engstruct.2021.112892.
[20] Ji J, Zhang Z, Lin M, Li L, Jiang L, Ding Y, Yu K. Structural application of engineered cementitious composites (ECC): a state-of-the-art review. Constr Build Mater 2023;406:133289. https://doi.org/10.1016/j.conbuildmat.2023.133289.
[21] Khalil AEA, Atta AM, Hassan A, Abd-Elaaty AH. Flexural strength recovery of RC one-way slabs having cut-outs using NSM-SHCC plates. Eng Struct 2022;258. https://doi.org/10.1016/j.engstruct.2022.114149.
[22] Wu C, Li VC. CFRP-ECC hybrid for strengthening of the concrete structures. Compos Struct 2017;178:372–82. https://doi.org/10.1016/j.compstruct.2017.07.034.
[23] Zheng YZ, Wang WW, Brigham JC. Flexural behaviour of reinforced concrete beams strengthened with a composite reinforcement layer: BFRP grid and ECC. Constr Build Mater 2016;115:424–37. https://doi.org/10.1016/j.conbuildmat.2016.04.038.
[24] Pan B, Liu F, Zhuge Y, Zeng JJ, Liao J. ECCs/UHPFRCCs with and without FRP reinforcement for structural strengthening/repairing: a state-of-the-art review. Constr Build Mater 2022;316:125824. https://doi.org/10.1016/j.conbuildmat.2021.125824.
[25] Zhu JX, Xu LY, Huang BT, Weng KF, Dai JG. Recent developments in engineered/strain-hardening cementitious composites (ECC/SHCC) with high and ultra-high strength. Constr Build Mater 2022;342:127956. https://doi.org/10.1016/j.conbuildmat.2022.127956.
[26] Zhu JX, Weng KF, Huang BT, Xu LY, Dai JG. Ultra-high-strength engineered cementitious composites (UHS-ECC) panel reinforced with FRP bar/grid: development and flexural performance. Eng Struct 2024;302:117193. https://doi.org/10.1016/j.engstruct.2023.117193.
[27] Zhu JX, Weng KF, Liu WH, Huang BT, Peng KD, Zhu JH, Dai JG. Thin-layer ultra-high-strength engineered cementitious composites (UHS-ECC) reinforced with small-diameter FRP bars for structural strengthening. Thin-Walled Struct 2024;205:112592. https://doi.org/10.1016/j.tws.2024.112592.
[28] Ellithy M, Hassan A, El-Shafiey TF. Flexural strengthening of RC beams using PGFRP bars embedded in strain-hardening cementitious composites (SHCC). Eng Struct 2024;317:118628. https://doi.org/10.1016/j.engstruct.2024.118628.
[29] Pan B, Liu F, Zhuge Y, Zeng JJ, Liao J. ECCs/UHPFRCCs with and without FRP reinforcement for structural strengthening/repairing: a state-of-the-art review. Constr Build Mater 2022;316:125824. https://doi.org/10.1016/j.conbuildmat.2021.125824.
[30] Ji J, Zhang Z, Lin M, Li L, Jiang L, Ding Y, Yu K. Structural application of engineered cementitious composites (ECC): a state-of-the-art review. Constr Build Mater 2023;406:133289. https://doi.org/10.1016/j.conbuildmat.2023.133289.
[31] PAGE CL. Mechanism of corrosion protection in reinforced concrete marine structures. Nature 1975;174:514–5. https://doi.org/10.1038/258514a0.
[32] Almusallam A. Effect of degree of corrosion on the properties of reinforcing steel bars. Constr Build Mater 2001;15:361–8. https://doi.org/10.1016/S0950061801)00009-5.
[33] Andrade C, Alonso C, Garcia D, Rodriguez J. Remaining lifetimes of reinforced concrete structures: effect of corrosion on the mechanical properties of the steel. Cambridge, UK: NACE; 1991. p. 546–57.
[34] Atta A, Ali N, Taman M. Efficiency and corrosion characteristics of high performance cementitious composites as a strengthening material. Compos Part B 2019;166:341–51. https://doi.org/10.1016/j.compositesb.2018.11.105.
[35] Elghazy M, El Refai A, Ebead U, Nanni A. Post-repair flexural performance of corrosion-damaged beams rehabilitated with fabric-reinforced cementitious matrix (FRCM). Constr Build Mater 2018;166:732–44. https://doi.org/10.1016/j.conbuildmat.2018.01.128.
[36] Hu B, Zhou Y, Xing F, Sui L, Luo M. Experimental and theoretical investigation on the hybrid CFRP-ECC flexural strengthening of RC beams with corroded longitudinal reinforcement. Eng Struct 2019;200:109717. https://doi.org/10.1016/j.engstruct.2019.109717.

[37] Triantafyllou GG, Rousakis TC, Karabinis AI. Corroded RC beams patch repaired and strengthened in flexure with fiber-reinforced polymer laminates. Compos Part B 2017;112:125–36. https://doi.org/10.1016/j.compositesb.2016.12.032.
[38] Sohail MG, Wasee M, Al Nuaimi N, Alnahhal W, Hassan MK. Behavior of artificially corroded RC beams strengthened with CFRP and hybrid CFRP-GFRP laminates. Eng Struct 2022;272:114827. https://doi.org/10.1016/j.engstruct.2022.114827.
[39] Daneshvar K, Moradi MJ, Ahmadi K, Hajiloo H. Strengthening of corroded reinforced concrete slabs under multi-impact loading: experimental results and numerical analysis. Constr Build Mater 2021;284:122650. https://doi.org/10.1016/j.conbuildmat.2021.122650.
[40] Cabrera JG. Deterioration of concrete due to reinforcement steel corrosion. Cem Concr Compos 1996;18:47–59. https://doi.org/10.1016/0958-9465(95)00043-7.
[41] Hou L, Liu H, Xu S, Zhuang N, Chen D. Effect of corrosion on bond behaviors of rebar embedded in ultra-high toughness cementitious composite. Constr Build Mater 2017;138:141–50. https://doi.org/10.1016/j.conbuildmat.2017.02.008.
[42] Şahmaran M, Li VC, Andrade C. Corrosion resistance performance of steel-reinforced engineered cementitious composites beams. Acids Mater J 2008;105:243–55.
[43] ASTM. standard C39/C39M. Standard Test Method for Compressive Strength of Cylindrical Concrete Specimens. West Conshohocken, PA, USA: Annual Book of ASTM Standards; 2021.
[44] ASTM C496/C496M. Standard Test Method for Splitting Tensile Strength of Cylindrical Concrete Specimens. West Conshohocken, PA, USA: Annual Book of ASTM Standards; 2017.
[45] Japan Society of Civil Engineers (JSCE). Recommendations for design and construction of high performance fiber reinforced cement composite with multiple fine cracks (HPFRCC). Concr Eng Ser 2008;82.
[46] ASTM E8/E8M-22. Standard Test Methods for Tension Testing of Metallic Materials. West Conshohocken, PA, USA: Annual Book of ASTM Standards; 2022.
[47] Ahmed S. Reinforcement corrosion in concrete structures, its monitoring and service life prediction-a review. Cem Concr Compos 2003;25:459–71. https://doi.org/10.1016/S0958-9465(02)00086-0.
[48] ASTM C876. Standard test method for corrosion potentials of uncoated reinforcing steel in concrete. 2015.
[49] ASTM. Standard practice for preparing, cleaning, and evaluating corrosion test specimens. ASTM-G1-03. West Conshohocken, PA: ASTM; 2011.
[50] Du YG, Clark LA, Chan AHC. Effect of corrosion on ductility of reinforcing bars. Mag Concr Res 2005;57(7):407–19. https://doi.org/10.1680/macr.2005.57.7.407.
[51] Etman EE, Mahmoud MH, Hassan A, Mowafy MH. Flexural behaviour of concrete beams reinforced with steel-FRP composite bars. Structures 2023;50:1147–63. https://doi.org/10.1016/j.istruc.2023.02.098.
[52] ACI Committee 318. Building Code Requirements for Structural Concrete (ACI 318-19) and Commentary (ACI 318R-19). Farmington Hills, MI: American Concrete Institute; 2019. p. 519.
[53] Egyptian code for design and construction of reinforced concrete structures (ECP 203-2020); 2020.